Impact of MU-MIMO on Passive Wi-Fi Radars: Threat or Opportunity?

Hasan Can Yildirim
OPERA-WCG
Université Libre de Bruxelles
Université Catholique de Louvain
Brussels, Belgium
hasan.can.yildirim@ulb.be

Laurent Storrer
OPERA-WCG
Université Libre de Bruxelles
Brussels, Belgium
laurent.storrer@ulb.be

Jerôme Louveaux
ICTM-ELEN
Université Catholique de Louvain
Louvain-la-Neuve, Belgium
jerome.louveaux@uclouvain.be

Philippe De Doncker
OPERA-WCG
Université Libre de Bruxelles
Brussels, Belgium
philippe.dedoncker@ulb.be

François Horlin
OPERA-WCG
Université Libre de Bruxelles
Brussels, Belgium
francois.horlin@ulb.be

***Abstract*—Passive Radars are devices that make use of existing communication signals for wireless channel sensing. On the other hand, Wi-Fi has become the main gateway that connects devices to the internet. Recently, IEEE established the WLAN Sensing Task Group whose purpose is to study the feasibility of Wi-Fi-based environment sensing, where some of the technologies share similarities with Passive Radars. In the meantime, Multi-User Multiple-Input Multiple-Output (MU-MIMO) technology is introduced to the Wi-Fi standard. It is designed to improve the spatial efficiency of the wireless channel by simultaneously transmitting directive Wi-Fi signals to users. This paper aims at quantifying the impact of MU-MIMO signals on Passive Wi-Fi-based Radar-like sensing. First, based on the position of the client devices and the channel geometry, the radiation pattern of the AP is derived. While the wireless channel is illuminated by directive radio waves, the magnitude of the Poynting vector is obtained at a local point target, which then reflects the incident radio waves. Finally, the signal power seen by a sensing device is computed under the influence of a multipath channel. Our numerical analyses focus on an urban street, and we show that MU-MIMO can be seen as; i) an opportunity, since the vicinity of client devices are better illuminated, or ii) a threat, since the remaining parts of the street do not receive sufficient amount of power for channel sensing applications.**

***Index Terms*—Passive Wi-Fi Radar, Passive Channel Sensing, MU-MIMO, probability of detection**

I. Introduction

Passive Radars (PR) are devices that detect and track humans and/or other objects by applying radar processing algorithms to opportunistically captured signals [1]. More specifically, Passive Wi-Fi-based Radars (PWRs) estimate the range, speed and Angle-of-Arrival (AoA) information from the OFDM symbols transmitted in Wi-Fi frames [2]. However, since the IEEE 802.11 Wi-Fi standard has ever been evolving, its frame and signal structures has to be well studied in order to evaluate the new opportunities and challenges that the standard brings to PWRs. The milestones of 802.11 standard, which uses only the sub-7 GHz spectrum, can be summarized as:

- *802.11a*: The Orthogonal Frequency-Division Multiplexing (OFDM) modulation was introduced to deal with frequency-selective wireless channels, for a maximum bandwidth of 20 MHz, making it possible to apply OFDM-based radar processing algorithms.
- *802.11n*: After a few evolutionary amendments, Multiple-Input Multiple-Output (MIMO) antenna configuration was introduced which enabled spatial diversity through 4 spatial streams. Also, PWRs started to receive an increased attention [3].
- *802.11ac*: The downlink MU-MIMO technology was introduced which increases the spatial efficiency by simultaneously transmitting data frames to multiple clients. Moreover, the number of spatial streams and maximum bandwidth were increased to 8 and 160 MHz (providing roughly 1 meter range resolution), respectively.
- *802.11ax*: Recently, uplink MU-MIMO and Orthogonal Frequency-Division Multiple Access (OFDMA) technologies are introduced, which further improve the spatial and spectral efficiency, respectively.
- *802.11be*: In the near future, the next evolutionary step of the Wi-Fi standard is going to bring even larger bandwidths (up to 320 MHz, roughly 0.5 meters range resolution), enhanced spatial diversity (maximum of 16 spatial streams), and possibly, coordinated and joint transmission by multiple Access Points (APs) [4].
- *802.11bf* IEEE formed the WLAN Sensing (WS) Task Group (802.11bf) whose goal is to introduce a Wi-Fi-based sensing scheme within the 802.11 standard [5].

The WS and PWR share similarities since both of them work with similar principles where OFDM-based channel estimation techniques are applied on Wi-Fi signals. However, WS provides a standardized framework where 802.11bf enabled devices can collaborate for channel sensing. In contrast, PWRs

work by only listening/receiving already transmitted Wi-Fi signals. Nonetheless, in [6], it is shown that the priorly known training fields in Wi-Fi frames can be used for PWR processing, without any need for reference signal reconstruction.

In the meantime, MU-MIMO is a technology that needs further attention since it is designed only for wireless communication purposes, but its impact on PWR is not yet addressed. In MU-MIMO the AP can form directive radio waves towards different client devices (STAs), while minimizing the interference among other STAs. To do so, an 802.11ax AP starts the channel sounding session (CSS) by isotropically transmitting the so-called Null Data Packet (NDP) [7]. Then, the STAs estimate their channels based on the received NDP and send it back to the AP. With the available explicit feedback, the AP can compute a precoding matrix and start the MU-MIMO data transmission. Therefore, the wireless channel is globally illuminated during CSS while MU-MIMO illuminates only the vicinity of STAs.

In this work, the impact of MU-MIMO on PWR processing is examined. In [8], the statistical coverage analysis of downlink MU-MIMO channel has been studied. Poisson Point Processes are used to model the position of mobile users and the APs, and a coverage probability is estimated. In [9], the coverage probability and achievable rate analysis are studied within a similar context, with the addition of fractional frequency reuse. The contribution of our work can be summarized as follows:

- By considering local point targets, frequency-selective channels, and directive radio waves, the two-way received signal power is derived for quasi-monostatic PWR geometry.
- To show the pros and cons of having MU-MIMO enabled during a PWR procedure, realistic numerical analyses are provided which takes place in an urban street.

This paper is structured as follows. In Section II, the system model is given for a MU-MIMO channel and the corresponding radiation pattern for a given subcarrier is obtained. In Section III, the received signal power and signal-to-noise-power-ratio (SNR) are derived. In Section IV, numerical results with various scenarios are provided to show the impact of MU-MIMO on the illumination of wireless channel. Finally, in Section V, the conclusion is drawn.

Notations: $\mathbf{H}_q \in \mathbb{C}^{M\times N}$ represents a matrix and $\mathbf{H}_q[m,n]$ is an entry on its mth row and nth column. Moreover, $\mathbf{H}_q[m,:]$ and $\mathbf{H}_q[:,n]$ are the mth row and nth column of matrix $\mathbf{H}_q$, respectively. $\|\mathbf{H}\|_2$ is the ℓ_2-norm of the matrix $\mathbf{H}$. Meanwhile, $\mathbf{H}^T$ corresponds to the transpose of matrix $\mathbf{H}$. Similarly, h^*, $\mathbf{h}^*$ and $\mathbf{H}^*$ correspond to conjugate of scalar h, and Hermitian transpose of the vector $\mathbf{h}$ and matrix $\mathbf{H}$, respectively. Finally, M, N and Q represent the number of STAs, number of Tx antennas at the AP, and the number of OFDM subcarriers, respectively.

II. System Model

We assume that an 802.11ax AP already transmitted an NDP frame for channel sounding. After OFDM synchronization, the STAs that will participate in the next MU-MIMO-enabled data transmission frame estimate their channel transfer functions (CTFs). Based on a given CTF, a Beamforming Feedback Matrix (BFM) is derived per STA[1], which is then used to obtain the precoding matrix at the AP. Finally, the radiation pattern per subcarrier is computed based on the corresponding precoding matrix.

The MU-MIMO channel matrix between the mth STA and nth Tx antenna of the AP on subcarrier q can be defined as

$$\mathbf{H}_q = \begin{bmatrix} H_q[1,1] & \dots & H_q[1,N] \\ \vdots & \ddots & \vdots \\ H_q[M,1] & \dots & H_q[M,N] \end{bmatrix}, \in \mathbb{C}^{M\times N}. \quad (1)$$

Since we assume that each STA is equipped with only one receive (Rx) antenna, the rows of $\mathbf{H}_q$ correspond to the CTF of individual STAs on subcarrier q.

A. Beamforming Feedback per STA

Once the channel is estimated, an STA can compute the singular value decomposition of its CTF. Then, the right-eigenvectors (spanning the AoA subspace) obtained from the singular value decomposition are transmitted back to the AP as BFMs. However, assuming that each STA is equipped with one Rx antenna, BFM of the mth STA per subcarrier q can be written as

$$\mathbf{v}_{q,m} = \mathbf{H}_q[m,:] / \left\|\mathbf{H}_q[m,:]\right\|_2 .$$

Hence, a BFM is simply the CTF on subcarrier q, normalized by its ℓ_2- norm as long as the STAs are equipped with one Rx antenna. Once the BFMs are obtained for all active subcarriers, the STA sends them back to the AP[2].

B. Precoder Matrix at the AP

Once the AP receives all BFMs from the M STAs, it stacks them on a matrix per subcarrier, such that

$$\mathbf{B}_q = \left[\frac{\mathbf{H}_q[1,:]}{\|\mathbf{H}_q[1,:]\|_2} \; \frac{\mathbf{H}_q[2,:]}{\|\mathbf{H}_q[2,:]\|_2} \; \dots \; \frac{\mathbf{H}_q[M,:]}{\|\mathbf{H}_q[M,:]\|_2} \right], \in \mathbb{C}^{N\times M}$$

In other words, $\mathbf{B}_q$ corresponds to $\mathbf{H}_q^T$ in (1), where all of its columns are independently normalized based on the ℓ_2 norms. The precoding matrix per subcarrier q is obtained through Zero-Forcing as follows

$$\mathbf{D}_q = \mathbf{B}_q \Big(\mathbf{B}_q^* \mathbf{B}_q \Big)^{-1}, \in \mathbb{C}^{N\times M}$$

where the interference among different STAs is minimized by orthogonalizing their BFMs [11].

[1]It should be pointed out that in 802.11bf, STAs do not transmit BFMs. Instead, each WS participant transmits the raw estimation data, i.e., channel frequency response, back to the AP.

[2]Depending on the values of N and Q, the size of the BFM can be very large. Therefore, STAs may quantize the information in BFM. However, the impact of the quantization is beyond the scope of this work, readers are referred to [10].

In the meantime, the array vector corresponding to the uniform linear array geometry provided in Fig. 1 is defined as a function of angle-of-departure (AoD) angle θ at Tx

$$\mathbf{r}(\theta) = \left[1 \; e^{j\pi\cos(\theta)} \; \dots \; e^{j\pi(N-1)\cos(\theta)}\right], \in \mathbb{C}^N$$

where the antenna spacing is half the carrier wavelength and each antenna is omnidirectional. The vector containing the complex symbols that will be sent to each STA on subcarrier q is refered to as $\mathbf{s}_q \in \mathbb{C}^M$ whose variance is $\sigma^2_{\mathbf{s}_q} = 1, \forall q$.

Finally, the array gain per subcarrier q at AoD angle θ [12] can be obtained as

$$G_q(\theta) = 4\pi \frac{\left|(\mathbf{D}_q\mathbf{s}_q)^*\mathbf{r}(\theta)\right|^2}{\int_\Omega \left|(\mathbf{D}_q\mathbf{s}_q)^*\mathbf{r}(\theta)\right|^2 d\Omega}. \tag{2}$$

where Ω corresponds to 4π steradian. Here, combining the precoder matrix with the data vector can simply be seen as a sum over the columns of precoder matrix without changing their amplitudes. When its Hermitian transpose is combined with the array vector, nulls and peaks will be obtained on certain θ values.

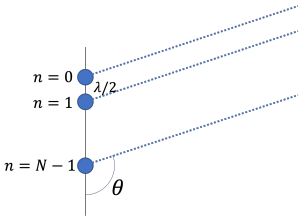

Fig. 1. Array geometry where antennas are separated by $\lambda/2$ meters.

III. Received Signal Power at Passive Radar

In this section, the received signal power is derived as a function of subcarrier q and the position of a local point target x. The AP is equipped with N antennas for data transmission, while the PWR device is equipped with a single antenna, closely located to the AP, i.e., quasi-monostatic geometry. Furthermore, all the antennas are omnidirectional in the horizontal plane and vertically polarized. Radio wave propagation is modelled by plane waves and all targets are assumed to be in the far-field. The wireless channel is split into two directions, namely

1) Forward channel (FC) which is defined as the wireless channel between the AP and the local point target at x. The transmitter power is set to unity ($P_{Tx} = 1$W) and the Tx array gain depends on the AoA as given in (2).
2) Backward channel (BC) which is defined as the wireless channel between the local point target and the PWR antenna. The backscatter power, i.e., the reflected signal power, is assumed to be equal to the incident power density (obtained in FC) multiplied by the Radar Cross Section (RCS) of a hypothetical target.

A. Forward Channel

Assuming that the AP is equipped with an array of vertically polarized and omnidirectional antennas, the total incident electric field at the local point target is expressed by [11]

$$E^i_q(x) = \sum_{l=0}^{L} a_{ql} \sqrt{\frac{2Z_0 G_q(\theta_l)}{4\pi}} \tag{3}$$

where L is the number of multipath components (MPCs), Z_0 is the impedance of vacuum, a_{ql} is the complex attenuation of MPC l, e.g., $a_{ql} = e^{-j\beta_q R_l}/R_l$ in Free Space. Here, θ_l and R_l correspond to the AoA and propagation distance of the lth path between the AP and the local point x, respectively. Moreover, in order to take into account the OFDM subcarriers, the wavenumber is defined as

$$\beta_q = \frac{2\pi}{c}(f_c + q\delta_f), \; q = 0, \dots, Q-1$$

where c is the speed of light in vacuum, f_c and δ_f are the carrier frequency and subcarrier spacing, respectively. The magnitude of Poynting vector at the local point is obtained as

$$S_q(x) = \frac{\left|E^i_q(x)\right|^2}{2Z_0}. \tag{4}$$

The reflectivity of target, often measured by its RCS σ, affects the magnitude of reflected radio waves. Hence, the power of reflected radio wave is $\sigma S_q(x)$ where σ is assumed to be omnidirectional.

B. Backward Channel

Similar to FC, the scattered electric field at the PWR device for a quasi-monostatic geometry can be expressed by

$$E^s_q(x) = \sum_{k=0}^{L} a_{qk} \sqrt{\frac{2Z_0 \sigma S_q(x)}{4\pi}} \tag{5}$$

where $a_{qk} = e^{-j\beta_q R_k}/R_k$ is the complex attenuation in BC, and R_k is the propagation distance of the kth path between the local point x and the PWR, respectively. Assuming that PWR is equipped with a single omnidirectional antenna, the received signal power can be written as

$$P_q(x) = \frac{\lambda_c^2}{4\pi} \frac{\left|E^s_q(x)\right|^2}{2Z_0} \tag{6}$$

where λ_c is the carrier wavelength and the first term corresponds to the antenna effective area. By using (3), (4) and (5) in (6), we obtain

$$P_q(x) = \frac{\lambda_c^2 \sigma}{(4\pi)^3} \left| \sum_{k=0}^{L} a_{qk} \right| \sum_{l=0}^{L} a_{ql} \sqrt{G_q(\theta^i_l)} \Bigg|^2. \tag{7}$$

The inner sum represents the magnitude of the Poynting vector at the target, caused by FC. The radiation pattern obtained in (2) is used for finding the array gain for each MPC. As seen, the amplitude of reflected signal can be decreased if the phases of the rays in FC cancel out each other. The outer sum, on the other hand, corresponds to BC where each MPC and their

phases are also taken into account. Since the PWR device is assumed to be equipped with a single omnidirectional antenna there is no array gain applied in BC. However, similar to FC, the sum over phase terms may yield a null, creating a blind-zone for the sensing device. By setting $L = 0$ in (7), i.e., by considering a Free Space channel where the distance between AP/PWR and a target is noted by R_0

$$P_q(x) = \frac{\lambda_c^2 \sigma}{(4\pi)^3} \frac{G_q(\theta_0)}{R_0^4}$$

is obtained which corresponds to the classical radar equation. Assuming that N_p coherent symbols/pulses are available for wireless channel sensing, the total SNR is computed by adding the magnitude of all subcarriers and dividing the result by the thermal noise of a given bandwidth [13], such that

$$\text{SNR}(x) = \frac{N_p \sum_{q=0}^{Q-1} P_q(x)}{kTBF}. \tag{8}$$

Here, $P_q(x)$ can be replaced by (7). Moreover, k corresponds to the Boltzmann constant while system terms T, B and F correspond to temperature in Kelvin, bandwidth and noise factor, respectively.

IV. Numerical Analysis

In this section, the impact of MU-MIMO is numerically assessed over a set of scenarios where the AP/PWR is located in an urban street as shown in Fig. 3. In order to derive the related MPC parameters, the Urban Canyon Model (UCM) is used with six-rays ($L = 6$, 1 LOS and its ground reflection, 2 first-order and 2 second-order reflections). The simulation procedure is described in Fig. 2, which works as follows. First, the CTF matrix $\mathbf{H}_q$ is obtained for a given set of AP and STA positions. Second, based on $\mathbf{H}_q$, the radiation pattern $\mathbf{G}_q$ is computed for all subcarriers. Third, the street topology is finely gridded into $0.1m \times 0.1m$ pieces. A hypothetical human target with $\sigma_{human} = -4$dBsm is placed on a grid node x and the corresponding channel parameters (θ_l and R_l) are obtained. Fourth, the SNR is computed for this target through (8), by taking into account all six-rays in both FC and BC. Once the third and fourth steps are repeated for all the grid nodes, a heat map of the entire scene can be obtained which shows the two-way SNR of hypothetical human targets placed on each grid node.

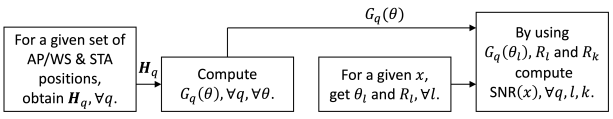

Fig. 2. The summary of simulation procedure. First two blocks are executed only once per realization to obtain the radiation pattern. The third and fourth blocks are repeated for all x positions. Once an SNR map of the entire scene is obtained, it can be translated into a PD map in a point-by-point fashion.

The probability of detection (PD) is considered as the main performance metric, which can be computed by numerically solving the Marcum's Q-function [14] for a given SNR and a probability of false alarm (PFa) as follows [13]

$$\text{PD}(a, b) = \int_b^\infty y \exp\big(-\frac{y^2 + a^2}{2}\big) I_0(ay) dy$$

where $a = \sqrt{2\text{SNR}(x)}$, $b = \sqrt{-2\ln(\text{PFa})}$, and I_0 is the modified Bessel function of the first kind of zero order. Independent from the considered application, PD levels should be as high as possible for a reliable detection system. In this work, the PD requirement is set to PD $\geq 90\%$ for any point target on the urban street.

In MU-MIMO, there are two types of Wi-Fi frame structures. First, the isotropically transmitted NDP where the number of available symbols is $N_p = N$, i.e., one training field per Tx antenna [7]. Second, the directive data frames that contain $N_p = N + N_d$ symbols where N training fields are followed by N_d data symbols. Since the number of available symbols has an impact on SNR, the difference between the two frame structures is taken into account by defining the following ratio $\Gamma = (N+N_d)/N$. Moreover, independent from the radiation pattern (whether it is isotropic or directive), the Effective Isotropic Radiated Power limit is set to 27 dBm at 5.6 GHz by the ETSI [ref]. Hence, during simulations, the transmit power is adjusted accordingly. Finally, the simulation parameters are summarized in Table I.

TABLE I
Summary of the Simulation Parameters

Parameter	Value	Unit
B	80	MHz
f_c	5.6	GHz
Q	1024	-
N	$4, 8, 16$	-
Γ	$2, 4, 8, 20$	-
PFa	10^{-7}	-
high-PD	PD $\geq 90\%$	-
σ_{human}	-4	dBsm
ϵ_{wall}	4	F/m

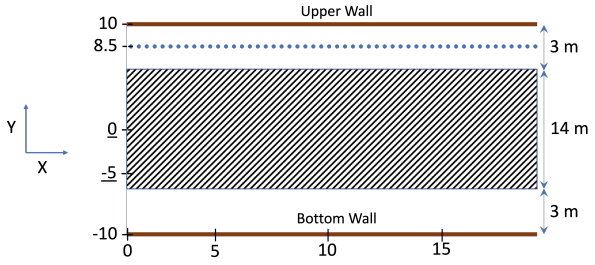

Fig. 3. UCM street topology with vehicle lane (grayed out area) and two pedestrian pavements (white areas). The street width is 20 meters and the walls are parallel to the X axis. Two underlined points on Y axis correspond to different AP/PWR positions, namely (0, 0) and (0, -5).

In Fig. 4, SNR and PD maps are shown on the upper and lower plots, respectively. The first column corresponds to

isotropic radiation pattern, i.e., during CSS, where the scene is globally illuminated. When the LOS path is sufficiently attenuated, i.e, the human target is further away from the AP/PWR pair, the destructive interference among MPCs decreases the SNR on local areas. The PD map further reveals that the decreased SNR causes blind zones for target detectability. The SNR/PD maps with directive radiation patterns, i.e., during MU-MIMO data transmission, are shown in the second column of Fig. 4. Since the STAs are well separated in space, most of the power is transmitted in the direction of LOS. Therefore, as shown in the PD map, the only global regions that are sufficiently illuminated are the ones around the LOS paths. Moreover, the sidelobes of the radiation pattern provide sufficient SNR on some regions closer to the AP/PWR pair, yielding detectable zones. However, local areas with reduced PD also appear closer to the walls because of the destructive interferences caused by reflections.

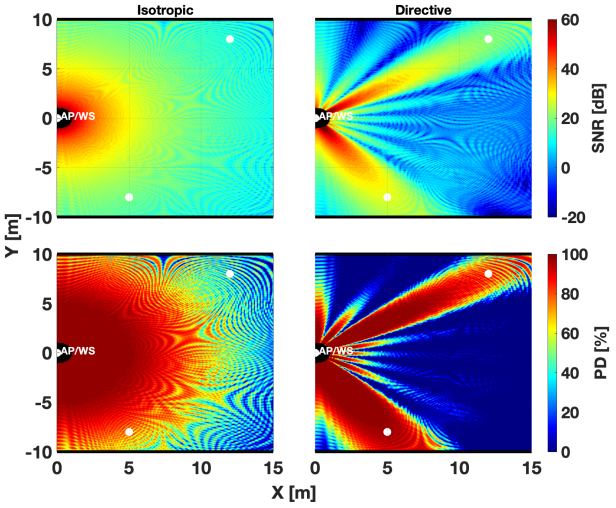

Fig. 4. Upper and lower plots correspond to SNR and PD maps, respectively. The white dots are the STAs. The AP/PWS pair is located at $(0, 0)$ and it is equipped with $N = 8$ antennas.

In Fig. 5, PD maps are provided to show the impact of the number of antennas N and the number of available OFDM symbols N_d. The first column shows the PD during CSS where the number of available OFDM symbols is limited by the number of Tx antennas. In this case, only a part of the bottom pavement reaches sufficient PD levels. As shown in the second and third columns, enabling MU-MIMO yields contrasting changes. First, the addition of beamforming gain limits the areas with sufficiently high PD but helps to highlight larger areas on the two pavements. Second, increasing the number of antennas, decreases the beam width. Hence, the size of global areas with sufficient PD becomes even smaller. Third, having more OFDM symbols improves the SNR and enlarges the radar coverage. One may argue that comparing isotropic and directive patterns while also changing the number of available symbols is not fair. However, we remind that in real-life, only N number of OFDM symbols are available in an NDP for channel estimation during CSS. In contrast, $N + N_d$ number of symbols are available during the directive data transmission stage.

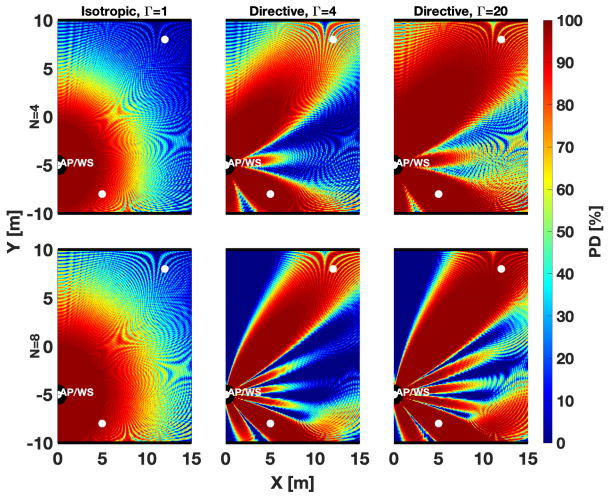

Fig. 5. Isotropic: during CSS. Directive: during MU-MIMO. Position of the AP/PWS pair is $(0, -5)$. From left-to-right, the corresponding N_d values are 0, 12 and 76, respectively.

In Fig. 6, only the PD values corresponding to the dotted line in Fig. 3 are plotted for two different upper-STA positions, (5, 8.5) and (15, 8.5). We can make the following observations which are common to all scenarios. First, when the upper-STA is further away, PD values around it and along the pavement drop due to the increased path loss and beamforming gain, respectively. Second, increasing N improves the spatial resolution and decreases the beam width. Hence, high-PD areas become smaller along the pavement. Third, increasing Γ improves SNR, which boosts the PD values and enlarges high-PD areas. Fourth, the interferences, caused by the reflections from walls create relatively large ripples across the pavement. These ripples vary the PD values as much as 40% in just a few centimeters. Moreover, when the upper-STA is 15 meters away, the amplitude variation of the ripples increases by the increased reflection angles and the decreased amplitude of LOS path. Additionally, when $N = 16$ and the upper-STA is 5 meters away, a high-PD zone appears between 6 and 10 meters. The reflected LOS path from the upper-wall creates this region, which still has a relatively larger amplitude to create a high-PD zone compared to other paths. Finally, negligible PD zones are created by the sidelobes around 0 meters when $N = 4, 16$ and around 10 meters when $N = 16$.

In order to show the impact of the position of AP/PWR on PD coverage, a set of plots are provided in Fig. 7 by varying only the position of AP/PWR, while the rest of the scenario remains unchanged. In this case, most of the previous observations still hold true: i) when the upper-STA is located further away, PD values drop due to the increased path loss; ii) increasing N, decreases the size of high-PD areas; iii) increasing Γ, boosts PD values all along the upper-pavement. In contrast with the previous scenario, the LOS path propagates over a larger distance to reach the upper-

STA. Consequently, PD variations appear all around the upper-pavement regardless of N and Γ values since all six paths have similar amplitude levels, i.e., LOS path does not dominate the remaining paths.

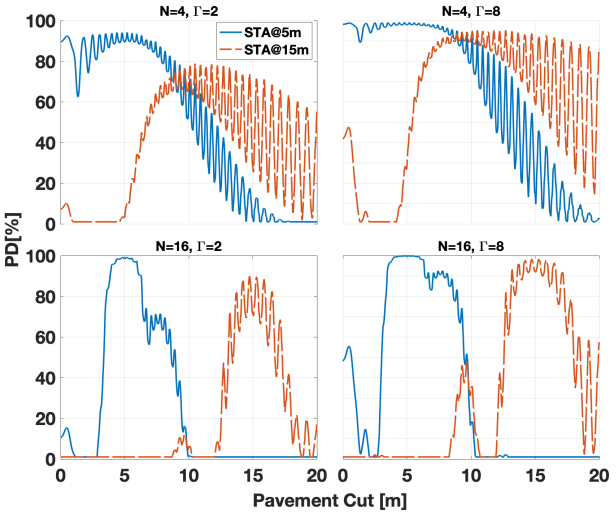

Fig. 6. AP/PWR at $(0, 0)$. Bottom-STA at $(10, -8.5)$. N and Γ increase over the rows and columns, respectively.

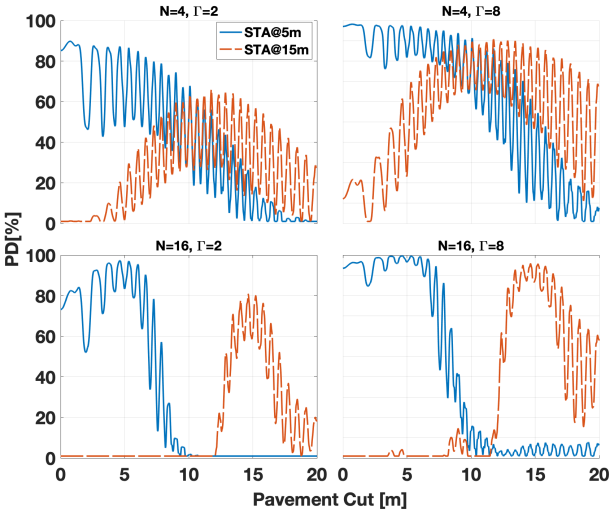

Fig. 7. AP/PWR at $(0, -5)$. Bottom-STA at $(10, -8.5)$.

V. Conclusion

In this work, we examined the impact of MU-MIMO on the PD coverage of Passive Wi-Fi-based Radars by deriving a deterministic two-way SNR model for a hypothetical human target placed in an urban street. Based on our analyses, enabling MU-MIMO does not have a black-and-white outcome for PWRs. First, isotropic radiation provides an equal coverage in the vicinity of AP/PWR pairs. However, depending on the AP/PWR placement and the width of street, it does not provide enough coverage on the pavements mainly due to the lack of symbols/pulses during CSS. Second, directive radiation provides high PD levels in the vicinity of STAs. However, depending on the STA positions and the number of antennas, some parts of the pavements do not reach to sufficient PD levels, while other parts are subject to high PD variations. When PWR is considered for pedestrian (or cars on traffic lanes) detection/tracking, a MU-MIMO enabled AP does not provide enough coverage for radar sensing. The two possible solutions, among many others, can be: i) deploying multiple PWR devices along pavements, which translates the scenario geometry from quasi-monostatic to multi-static while increasing the cost and complexity of the system, and ii) PHY or MAC layer algorithms to control the PD coverage even if MU-MIMO is enabled. Considering all these issues, it is evident that MU-MIMO and its impact on PWR requires further attention in order to guarantee a reliable radar coverage.

References

[1] Hugh Griffiths; Christopher Baker, "An Introduction to Passive Radar" , Artech, 2017.

[2] C. R. Berger, B. Demissie, J. Heckenbach, P. Willett and S. Zhou, "Signal Processing for Passive Radar Using OFDM Waveforms," in IEEE Journal of Selected Topics in Signal Processing, vol. 4, no. 1, pp. 226-238, Feb. 2010, doi: 10.1109/JSTSP.2009.2038977.

[3] P. Falcone, F. Colone and P. Lombardo, "Potentialities and challenges of WiFi-based passive radar," in IEEE Aerospace and Electronic Systems Magazine, vol. 27, no. 11, pp. 15-26, November 2012, doi: 10.1109/MAES.2012.6380822.

[4] C. Deng et al., "IEEE 802.11be Wi-Fi 7: New Challenges and Opportunities," in IEEE Communications Surveys & Tutorials, vol. 22, no. 4, pp. 2136-2166, Fourthquarter 2020, doi: 10.1109/COMST.2020.3012715.

[5] Yongsen Ma, Gang Zhou, and Shuangquan Wang, "WiFi Sensing with Channel State Information: A Survey". 2019, 52, 3, Article 46 (July 2019), 36 pages. DOI:https://doi.org/10.1145/3310194

[6] H. C. Yildirim, L. Storrer, M. V. Eechkhaute, C. Desset, J. Louveaux and F. Horlin, "Passive Radar based on 802.11ac Signals for Indoor Object Detection," 2019 16th European Radar Conference (EuRAD), 2019, pp. 153-156.

[7] Aruba Networks, "White Paper 802.11ax", www.arubanetworks.com/assets/wp/WP_802.11AX.pdf, Last accessed: 24/11/2021.

[8] A. Arsal, M. R. Civanlar and M. Uysal, "Coverage Analysis of Downlink MU-MIMO Cellular Networks," in IEEE Communications Letters, vol. 25, no. 9, pp. 2859-2863, Sept. 2021, doi: 10.1109/LCOMM.2021.3089663.

[9] S. Kumar, S. Kalyani, L. Hanzo and K. Giridhar, "Coverage Probability and Achievable Rate Analysis of FFR-Aided Multi-User OFDM-Based MIMO and SIMO Systems," in IEEE Transactions on Communications, vol. 63, no. 10, pp. 3869-3881, Oct. 2015, doi: 10.1109/TCOMM.2015.2465907.

[10] S. Jacobsson, G. Durisi, M. Coldrey, T. Goldstein and C. Studer, "Quantized Precoding for Massive MU-MIMO," in IEEE Transactions on Communications, vol. 65, no. 11, pp. 4670-4684, Nov. 2017, doi: 10.1109/TCOMM.2017.2723000.

[11] Clerckx, Bruno, and Claude Oestges. "MIMO Wireless Networks: Channels, Techniques and Standards for Multi-antenna, Multi-user and Multi-cell Systems", 2nd ed. Academic Press, 2013.

[12] Constantine A Balanis, "Antenna Theory: Analysis and Design", 3rd ed. Hoboken, NJ: John Wiley, 2005.

[13] M.A. Richards, J.A. Scheer, J. Scheer "Principles of Modern Radar: Basic Principles", ISBN: 9781891121524, Institution of Engineering and Technology, 2010.

[14] D. A. Shnidman, "The calculation of the probability of detection and the generalized Marcum Q-function," in IEEE Transactions on Information Theory, vol. 35, no. 2, pp. 389-400, March 1989, doi: 10.1109/18.32133.

[15] ETSI 301 893, "5 GHz RLAN; Harmonised Standard covering the essential requirements of article 3.2 of Directive 2014/53/EU", https://www.etsi.org/technologies/broadband-wireless-access, Last accessed: 24/11/2021.